

AFM Probing of Polymer/Nanofiller Interfacial Adhesion and Its Correlation with Bulk Mechanical Properties in a Poly(ethylene terephthalate) Nanocomposite

Shigeru Aoyama,^{†,||} Yong Tae Park,^{†,⊥} Christopher W. Macosko,[†] Toshiaki Ougizawa,[§] and Greg Haugstad^{*,‡}

[†]Department of Chemical Engineering and Materials Science, University of Minnesota, 421 Washington Avenue S.E., Minneapolis, Minnesota 55455, United States

[‡]Characterization Facility, College of Science and Engineering, University of Minnesota, 100 Union Street S.E., Minneapolis, Minnesota 55455, United States

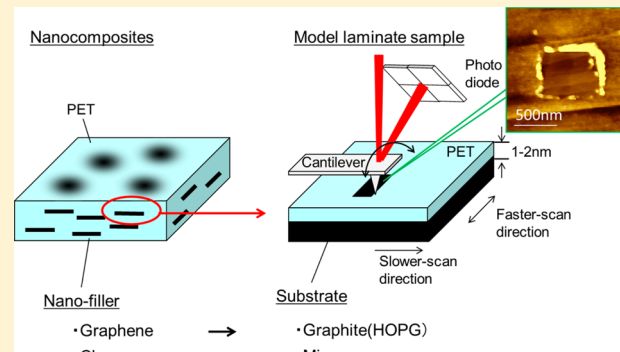
[§]Department of Chemistry and Materials Science, Tokyo Institute of Technology, 2-12-1-S8-33, O-okayama, Meguro-ku, Tokyo 152-8552, Japan

^{||}Films & Film Products Research Laboratories, Toray Industries, Inc., 1-1-1 Sonoyama, Otsu, Shiga 520-8558, Japan

[⊥]Department of Mechanical Engineering, Myongji University, First Engineering Bldg., 116 Myongji-ro, Cheoin-gu, Yongin, Gyeonggi-do 449-728, Korea

Supporting Information

ABSTRACT: The interfacial adhesion between polymer and nanofiller plays an important role in affecting the properties of nanocomposites. The detailed relationship between interfacial adhesion and bulk properties, however, is unclear. In this work, we developed an atomic force microscopy (AFM)-based abrasive scanning methodology, as applied to model laminate systems, to probe the strength of interfacial adhesion relevant to poly(ethylene terephthalate) (PET)/graphene or clay nanocomposites. Graphite and mica substrates covered with ~2 nm thick PET films were abrasively sheared by an AFM tip as a model measurement of interfacial strength between matrix PET and dispersed graphene and clay, respectively. During several abrasive raster-scan cycles, PET was shear-displaced from the scanned region. At temperatures below the PET glass transition, PET on graphite exhibited abrupt delamination (i.e., full adhesive failure), whereas PET on mica did not; rather, it exhibited a degree of cohesive failure within the shear-displaced layer. Moreover, 100-fold higher force scanning procedures were required to abrade through an ultimate “precursor” layer of PET only ~0.2–0.5 nm thick, which must be largely disentangled from the matrix polymer. Thus, the adhesive interface of relevance to the strength of clay–filler nanocomposites is between matrix polymer and strongly bound polymer. At 90 °C, above the bulk PET glass transition temperature, the PET film exhibited cohesive failure on both graphite and mica. Our results suggest that there is little difference in the strength of the relevant interfacial adhesion in the two nanocomposites within the rubbery dynamic regime. Further, the bulk mechanical properties of melt mixed PET/graphene and PET/clay nanocomposites were evaluated by dynamic mechanical analysis. The glassy dynamic storage modulus of the PET/clay nanocomposite was higher than that of PET/graphene, correlating with the differences in interfacial adhesion probed by AFM.



INTRODUCTION

Polymer nanocomposites are engineered by incorporating nanoscale fillers to modify properties relative to a pure polymer matrix. Two-dimensional platelet nanofillers outperform spherical nanofillers in the enhancement of mechanical and gas-barrier properties as well as dimensional stability.^{1,2} Modified clay^{3–8} and graphene^{9–16} are widely used as platelet nanofillers. Given its high modulus (250¹⁷–1000 GPa¹⁸) and electrical conductivity, graphene in particular has attracted considerable attention.^{11,14,16}

Nanocomposites are affected by the shape and properties of nanofillers, the degree of dispersion in the polymer matrix, and the strength of interfacial adhesion between polymer and nanofiller. Various methods have been proposed to measure interfacial adhesion. The most popular is fiber pull-out,^{19–21} which uses a single fiber in the matrix and records the load

Received: June 29, 2014

Revised: August 29, 2014

Published: October 6, 2014

during pull-out. Raman spectroscopy also has been widely used to investigate the stress transfer between matrix polymer and filler for a range of polymer nanocomposites.^{22–26} However, these two methods are limited in application to certain materials: the pull-out method is only applicable to fiber-shaped fillers, and Raman spectroscopy is only applicable to Raman-active materials.^{22–26}

Atomic force microscopy (AFM) is known as a powerful tool for probing nanoscale topography and mechanical properties. Several methods to probe interfacial adhesion in nanocomposites using AFM have been proposed.^{27–30} Barber et al.²⁷ conducted nanopull out measurements using a multiwall carbon nanotube attached to an AFM tip and obtained interfacial adhesion information. This technique is only appropriate for nanotube-shaped filler materials. Cai et al.²⁸ laminated sheets of two different polymers with graphene at the interface then peeled the sheets apart. AFM topographic images of both failure interfaces determined which polymer surface retained adhered graphene as a qualitative indicator of higher interfacial adhesion. Dvir et al.^{29,30} evaluated wear behavior of absorbed polyethylene and polypropylene layers (10–50 nm thick) on glass by contact-mode AFM scanning at variable applied force. They assumed that the threshold applied force for complete removal of polymer scaled with the strength of interfacial adhesion. They correlated the adhesion strength to different surface treatments of the glass but not to bulk nanocomposite properties.^{29,30} Moreover, polymer films less than 10 nm thick could not be investigated using their coating method, and thus the relative role of interfacial adhesion may have been suppressed.³⁰ Furthermore, these methods were only applied at room temperature.

The purpose of the present work is to (i) develop an AFM-based methodology to probe and to quantitatively model interfacial adhesion between matrix polymer and platelet-like nanofillers, both below and above the matrix polymer's glass transition temperature, T_g , and (ii) to assess the relationship between the adhesion as probed in (i) and measured bulk properties in the corresponding polymer nanocomposites. In order to probe polymer/platelet interfacial adhesion, we explore the friction and wear of ultrathin polymer films on model substrates during contact-mode AFM raster scanning. We focus on poly(ethylene terephthalate) (PET)-based nanocomposites due to its use in many industrial applications such as fibers, films, and bottles;³¹ moreover, PET-based nanocomposites have shown strong potential in various applications.^{4–6,13,14} PET resin is usually extruded into sheets followed by additional processing such as tenting and annealing above T_g .^{32–36} Additionally, products such as electrical parts and packaging are often exposed to temperatures higher than T_g during usage. Given that elevated temperature is relevant to both processing and performance, understanding interfacial adhesion below and above T_g is clearly of interest. PET films (1–2 nm thick) were deposited on highly oriented pyrolytic graphite (HOPG) and mica to model the PET/graphene and PET/clay interfaces in nanocomposites, respectively. Wear response was characterized in two temperature regimes, below T_g at 30–40 °C and above at 90 °C. PET/graphene and PET/clay nanocomposites were also prepared by melt mixing and melt pressing, and the mechanical properties of these bulk materials were evaluated by dynamic mechanical analysis (DMA). The results on nanocomposites are compared to the AFM-based abrasion results on the model film/substrate systems.

EXPERIMENTAL DETAILS

Materials. *Nanocomposites.* PET pellets provided from Toray Plastics America (North Kingstown, RI) were ground into powder (30 mesh particle size) by Polyvision (Manchester, PA). The intrinsic viscosity of PET powder after grinding was 0.61 dL/g (in *o*-chlorophenol), and its glass transition temperature was 78.8 °C by differential scanning calorimetry. Multilayered graphene and clay were used as nanofillers. Graphene 1 (G1) (XG Science, xGnP-C750, thickness 2 nm, diameter <2 μm, C/O = 3.2/1 by X-ray photoelectron spectroscopy) was used as received. Clay 1 (C1) (Southern Clay Products, Cloisite Na⁺, diameter <25 μm), a natural sodium montmorillonite, was also used as received. PET powder, graphene, and clay were dried in a vacuum oven at 120 °C for more than 12 h, and then PET/nanofiller mixtures of 5.5 g with different loading (from 0 to 12 wt % for PET/G1 and from 0 to 16 wt % for PET/C1) were fed into a recirculating twin screw extruder (Microcompounder, DACA Instruments) at 280 °C with N₂ purge. The components were mixed at 360 rpm for 8 min then extruded into an ice/water bath for cooling.

Rheological measurements were carried out with a rotational rheometer (ARES, TA Instruments) at 270 °C under a N₂ atmosphere. 0.6–0.7 g of the extruded nanocomposites was dried at 120 °C for at least 12 h and then loaded between 25 mm parallel plates. They were squeezed into disks ~1 mm thick by slowly lowering the upper plate. Using a dynamic strain sweep at 1 rad/s, the critical strain, γ_{crit} , where storage modulus, G' , drops to 90% of its limiting low strain value was recorded. Then the dynamic moduli were measured at $\gamma < \gamma_{crit}$ from 100 to 0.1 rad/s.

The dynamic tensile moduli of the polymer/nanofiller nanocomposites were evaluated using a Rheometrics Solid Analyzer, RSA-G2 (TA Instruments, New Castle, DE) at 1 Hz and several temperatures on 120–180 μm thick films obtained by pressing the dried extruded samples between fiber reinforced Teflon sheets at 270 °C at 1–1.5 MPa for 2 min and then quenched in ice water to minimize crystallization. Microtomed sections of these films were imaged using a FEI Tecnai T12 transmission electron microscope. Detailed TEM specimen preparation and imaging parameters are reported elsewhere.³⁷

Films and Substrates. HOPG and mica were used for AFM work as models for graphene and clay, respectively. HOPG (K-Tek Nanotechnology LLC., GRBS/1.2, ZYB Quality) and mica (SPI Supplies, 01868-CA, grade V-1), as received, were freshly cleaved just prior to the deposition of films by spin-coating. 1,1,1,3,3-Hexafluoro-2-propanol (HFIP; Sigma-Aldrich) and chloroform (Sigma-Aldrich) were used as solvents. PET was dissolved in the above-described HFIP/chloroform = 3/2 (w/w) at a concentration of 0.005 wt % for deposition on HOPG and dissolved in HFIP at a concentration of 0.1 wt % for deposition on mica. (Pure HFIP and higher concentration were used because the HFIP/chloroform = 3/2 (w/w) solution fully dewetted on mica, preventing the formation of thin films.) Each solution was stirred until clear (>2 h). A drop of solution was spin-coated onto a given substrate and then dried on a hot plate at 60 °C for 5 min and in a vacuum oven at 120 °C for more than 12 h. Films were further annealed on a hot plate at 270 °C for 1 min to cancel the processing history and then quenched in ice water to minimize crystallization. Film thicknesses of 1–2 nm resulted from the above process, as determined from abrasive AFM scanning and imaging, which is very close to the thickness of the interface region in both thin films as reported by Kim et al.³⁸ and bulk nanocomposites as reported by Sargsyan et al.³⁹ Therefore, in this study we consider 2 nm thick polymer films on mica and HOPG substrates to be representative of the filler–matrix interfacial domains in bulk nanocomposites. Over ~1 μm scale regions (i.e., somewhat larger than the size of abrasive raster scans), PET film thickness on HOPG and mica ranged (highest peak to deepest valley) by 0.8 and 0.6 nm, respectively, and had arithmetic roughnesses (R_a) of approximately 0.15 nm.

AFM Instrumentation. AFM imaging and measurements were performed in a N₂ atmosphere (RH < 1%) using an environmental scanning probe microscope, Agilent 5500 (Agilent Technology, Santa

Clara, CA), running Picoview software and interfaced with the Digital Pulsed Force Mode add-on hardware/software package (DPFM, WITec, Ulm, Germany), which images a surface via fast force-distance curve mapping (also known as “peak force tapping” as implemented by another vendor).⁴⁰ DPFM was used for assessment (i.e., nonperturbative imaging of topography with minimal shear, at a maximum applied normal force of about 1.5 nN and at 2 Hz scan frequency, operating at 2 kHz of Z cycling frequency and approximately 35 nm of Z cycling range) before and after abrasive scanning. DPFM was also used for materials contrast via tip–sample adhesion images (i.e., pull-off force per force–distance cycle), whereas contact mode was used for abrasive scanning. All AFM was performed using an Agilent piezosscanner operated in closed loop in X–Y (90 μm range) but open loop in Z (6 μm range). Sample temperature was achieved using a resistively heated commercial sample stage (Agilent) and a Lakeshore temperature controller. An uncoated silicon tip/cantilever (AppNano FORT) with a measured spring constant of 0.21 N/m and nominal radius of curvature of 10 nm was used for all results reported herein. (Fine force sensitivity, not large force range, was required for the main body of this study.) Nominally similar tips/cantilevers reproduced the basic findings in a larger body of experiments not reported here. The cantilever spring constant was calibrated using force curves obtained by pressing the tip near the end of a precalibrated tipless reference cantilever (AppNano FCL) and evaluating the ratio of force-curve contact slope to that on a rigid Si substrate.⁴⁰ The deflection measurement inverse sensitivity, 0.24 nm/mV, was calibrated from the contact slope of force curves on a rigid bare substrate.

AFM Friction and Abrasion Measurements Method. Multiple raster scans were performed over a given film region at high load to abrasively displace the polymer film from the scanned region via shear forces, as depicted in Figure 1. Lateral forces were measured, under

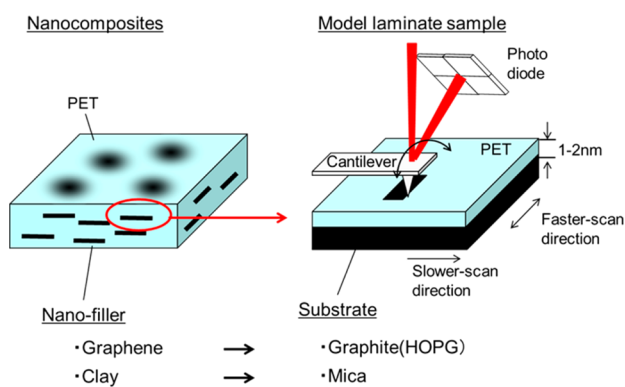


Figure 1. Schematic for probing interfacial adhesion between polymer and fillers in nanocomposites by performing abrasive AFM raster scanning of a model film/substrate system.

fixed normal (vertical) force load, via the split (quad) photodiode scheme that is standard to commercial AFMs; here both twisting and bending of the cantilever are quantified and thereby lateral and normal forces on the AFM tip, respectively. Both topography and trace and retrace lateral force images (derived from left-to-right and right-to-left scans) were acquired simultaneously in contact mode over the entire raster-scanned region and reported herein (without cropping). Subsequently, a friction force (F_f) image (with topographic slope effects, i.e., conservative forces, largely removed) was obtained by subtracting each corresponding pixel datum of the retrace lateral force from trace lateral force and dividing by 2.⁴⁰ A total of 512 fast-scan cycles (i.e., a left-to-right scan followed by a right-to-left scan) at a cycling frequency of 4 Hz were executed per each 500 \times 500 nm raster scan during abrasive scanning at elevated applied forces of 5–15 nN. These applied forces are only the vertical forces with which the tip is pressed against the sample and correlate to the frictional shear forces that (primarily) displace the PET during abrasive scanning (i.e.,

friction increases with applied load). Five of these raster scans were performed in succession on each abrasion region. Friction force was quantified from a histogram of F_f per friction force image (see Figure S1 in Supporting Information). The lateral force measurement was calibrated (1.36 nN/mV) by scanning a topographic region (a thicker PET film domain on mica) with strongly variable slope along the fast scan axis at 1.5 nN applied force, given a preceding calibration of vertical force.⁴⁰ This procedure also produced a measurement of coefficient of friction on PET films, 0.37, during low-load nonabrasive scanning, whereas this coefficient was found to approach or even exceed unity during abrasive scanning procedures (reflecting the strong dissipation of macromolecular disentanglement and in some cases detachment from substrate).

RESULTS AND DISCUSSION

Morphology of PET Films on HOPG and Mica.

Representative 5 \times 5 μm topographic and tip–sample adhesion images of PET films on HOPG and mica substrates at 30 °C, prior to abrasive scanning over smaller subdomains, are shown in Figure 2. On HOPG the location of larger substrate steps is

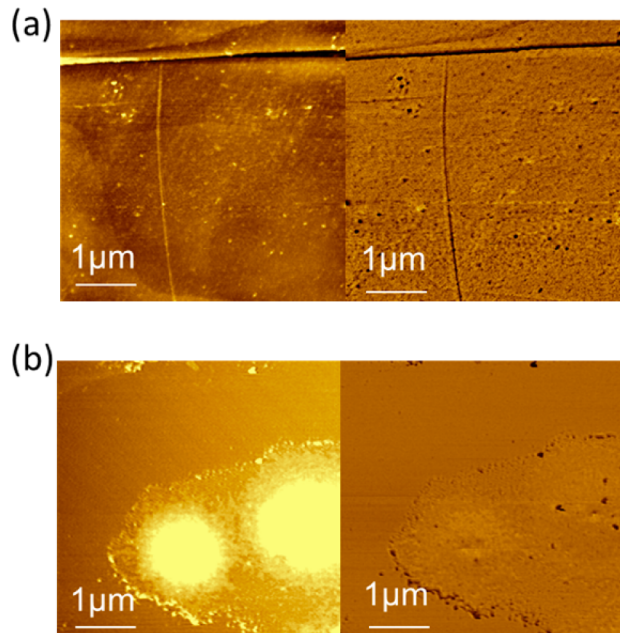


Figure 2. Representative topography images (left) and tip–sample adhesion images (right) of PET films on (a) HOPG and (b) mica. The difference in surface elevation between the brightest and darkest features per image is (a) 6 nm and (b) 10 nm.

visible as near-linear features in both height and adhesion. (These large steps were avoided during later abrasion procedures.) On mica autophobic dewetting is observed:⁴¹ a 0.2–0.5 nm thick, strongly bound monolayer completely covers the mica⁴² (as assessed in subsequent abrasion procedures, exemplified in Figures S2 of the Supporting Information), whereas taller domains have dewetted from the first layer. Portions of the images in Figure 2b (e.g., at and slightly above center) contain a relatively thin (~2 nm) second layer (the top ~third of the image being the first, precursor layer), the site of abrasion procedures reported herein, whereas the lower middle and right portions of the images in Figure 2b contain thicker domed regions (~10 nm) that were avoided during abrasive scanning. The adhesion images in each image pair further contain laterally small (~100 nm) domains of extremely low adhesion, likely moieties of high PET crystallinity.

Representative $1.5 \times 1.5 \mu\text{m}$ topography and tip–sample adhesion images, as well as single-line height profiles, are shown in Figure 3 following abrasive raster scanning of $0.5 \times 0.5 \mu\text{m}$

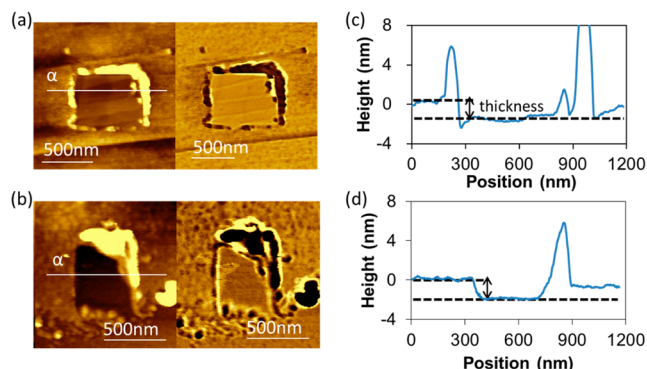


Figure 3. Representative topography images (left) and tip–sample adhesion images (right) of PET layers at 30°C on (a) HOPG and (b) mica following abrasive scanning in a $500 \times 500 \text{ nm}$ subdomain. Topographic cross-sectional profiles are shown in (c) and (d), corresponding to the line segments marked in (a) and (b). The difference in surface elevation between the brightest and darkest features is (a) 8 nm and (b) 6 nm.

subdomains (treated in detail in the next section). The topography and adhesion in the modified domains of each film indicate that the polymer film has been removed either largely (on mica, leaving the 0.2 nm bound film⁴² in this case) or completely (on HOPG). Thus, relevant film thickness is quantified in each case and is approximately 2 nm. At the periphery of each abraded domain (especially around the upper right quadrant of each) lie tall mounds not present prior to abrasion, indicating PET that has been displaced to the edge of the raster-scanned domain. Correspondingly low tip–sample adhesion is also observed atop these mounds, indicating a tendency for the displaced PET to crystallize, a not-uncommon observation for crystallizable polymers.⁴³

Filler Effects of Interfacial Adhesion of PET Thin Layer on Substrate.

In this section we present and discuss

observations made during the abrasive raster scan process. Multiple raster scans were performed over a given film region at fixed loading forces (5, 10, and 15 nN) to abrasively displace the PET film from the substrate via shear forces (Figures 4 and 5). During several abrasive raster scans on PET/HOPG at 5 and 10 nN as shown in Figure 4, bundles/mounds of PET grew in height and tended to collect near the center of the scanned domain, gradually baring larger substrate areas as inferred from the smooth character of (and shallow steps in) such subregions. The same raster scanning at 15 nN of applied force left what appears to be bare substrate even after the very first raster scan, indicating that the PET film was completely shear-displaced from the scanned region. This suggests that PET on HOPG exhibited abrupt delamination (i.e., full adhesive failure) during raster scanning at 15 nN.

The same abrasive raster scanning procedure on PET/mica exhibited notably different behavior as exemplified in Figure 5. Stark bundles/mounds of the PET were less visible at all forces up to the shown results at an applied load of 15 nN. Clearly the mica substrate was not bared even after five raster scans, in contrast to the behavior of PET/HOPG, suggesting cohesive failure rather than abrupt delamination. Subsequent topography and tip–sample adhesion images over a larger region containing the abrasively scanned subregion indicate the baring of HOPG (Figure 6a), whereas some areas in the scanned region on mica were still covered by PET film (Figure 6b).

Friction forces, F_f , during abrasion scanning were obtained from the simultaneously acquired lateral force images as described in the Experimental Details and shown in Figures S1 and S3 of the Supporting Information. At 30°C , histograms of F_f on PET films on HOPG exhibited a broad distribution during the first abrasion raster scan but very narrow distributions during subsequent scans and strongly shifted to lower friction, with little change from scans 2–5. These results imply that the PET film on HOPG was shear-displaced from the scanned region at the first abrasion, baring the HOPG. On the other hand, histograms of F_f on PET on mica shifted more gradually to lower F_f but remained broader and with a higher average than on HOPG. These results suggest an incomplete

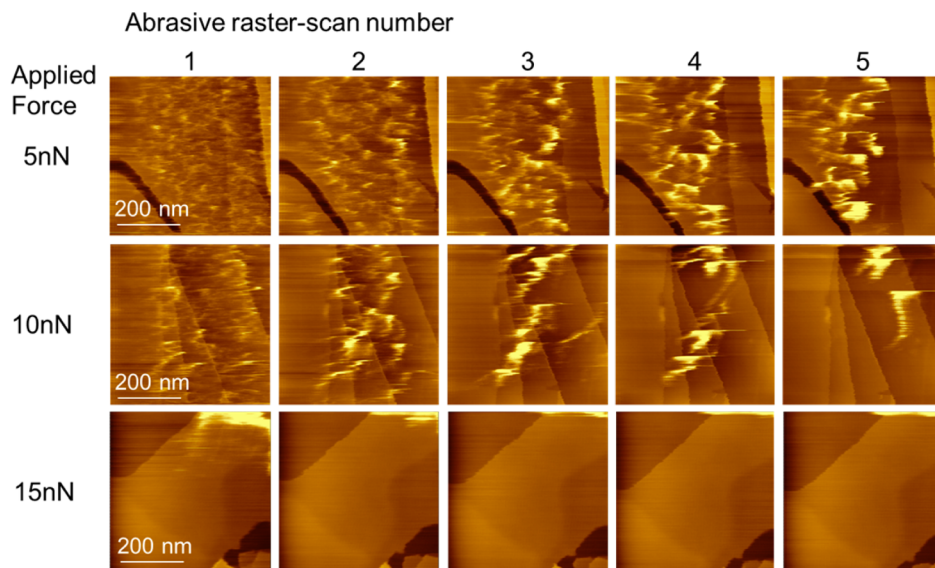


Figure 4. Representative $500 \times 500 \text{ nm}$ topography images of PET/HOPG during abrasive scanning at elevated applied forces. The difference in surface elevation between the brightest and darkest features is 6 nm.

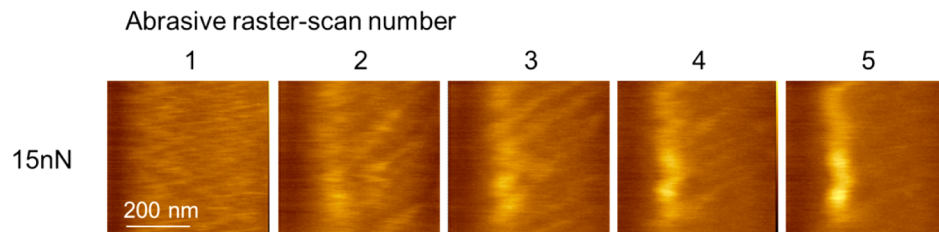


Figure 5. Representative topography images of PET/mica during abrasive raster scans at 15 nN applied load and 30 °C. The difference in height between the brightest and darkest features is 6 nm.

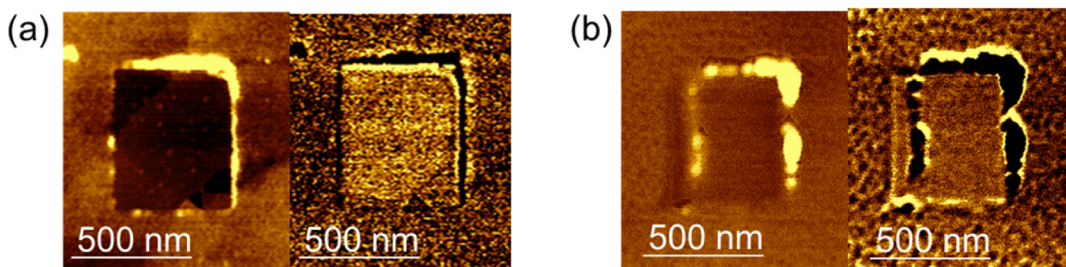


Figure 6. Representative nonperturbative topography images (left) and tip–sample adhesion images (right) of PET on (a) HOPG and (b) mica following five 500 nm abrasive raster scans at 15 nN applied load and 30 °C. The difference in surface elevation between the brightest and darkest features is 6 nm.

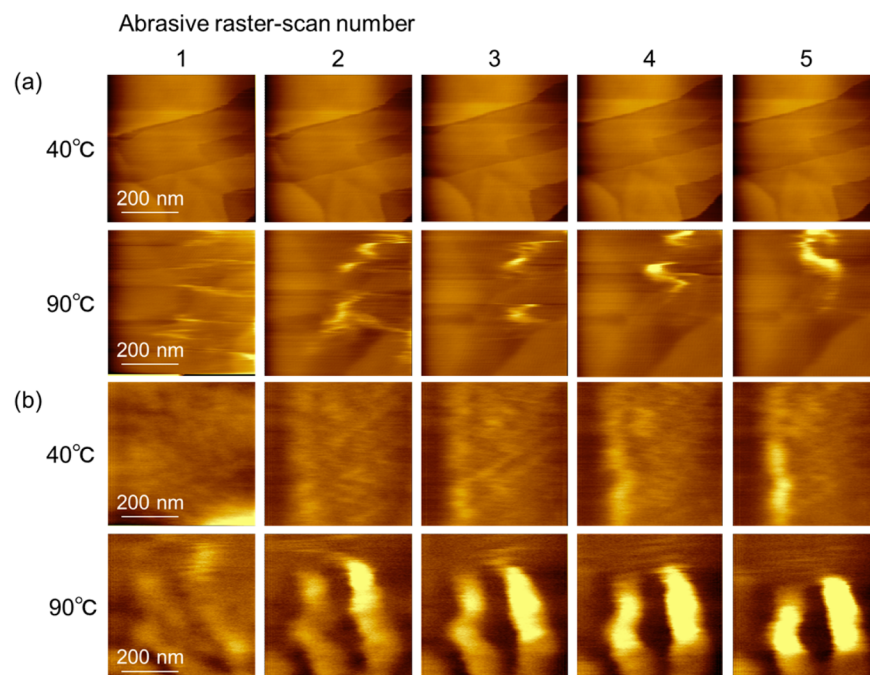


Figure 7. Five successive topography images 1–5 of (a) PET/HOPG and (b) PET/mica during abrasive scanning at a loading force of 15 nN and at temperatures below and above T_g . The difference in surface elevation between the brightest and darkest features is 6 nm.

baring of the mica substrate, consistent with the comparison of Figure 5 to Figure 4, and with our earlier statements that a 0.2–0.5 nm strongly bound layer of PET could only be removed by going to microneutron-regime forces (during force curve measurement mode, out of feedback) (see Figure S2.1 in the Supporting Information).

We found it useful to compute the difference between a given measured friction force during abrasive scanning, $F_f(\text{abrasion})$, and on a corresponding “bared” region (meaning bare HOPG or with only the 0.2 nm precursor PET layer left on mica, respectively), $F_f(\text{“bared”})$, defined as

$$\Delta F_{\text{Friction}} = F_f(\text{abrasion}) - F_f(\text{“bared”}) \quad (1)$$

This procedure and “bared” regions are exemplified in Figures S4–S6 of the Supporting Information. $\Delta F_{\text{Friction}}$ is plotted against the abrasive raster-scan number in Figure S7 (results are also plotted in Figure 9 in later session). $\Delta F_{\text{Friction}}$ of PET/HOPG was slightly lower than that of PET/mica at the first abrasion at 30 °C, and it became almost zero during the second abrasion. Meanwhile, $\Delta F_{\text{Friction}}$ of PET/mica gradually decreased with subsequent scan but did not decrease to zero even after the fifth abrasion. These results suggest that the interfacial adhesion between the thicker, partially dewetted PET

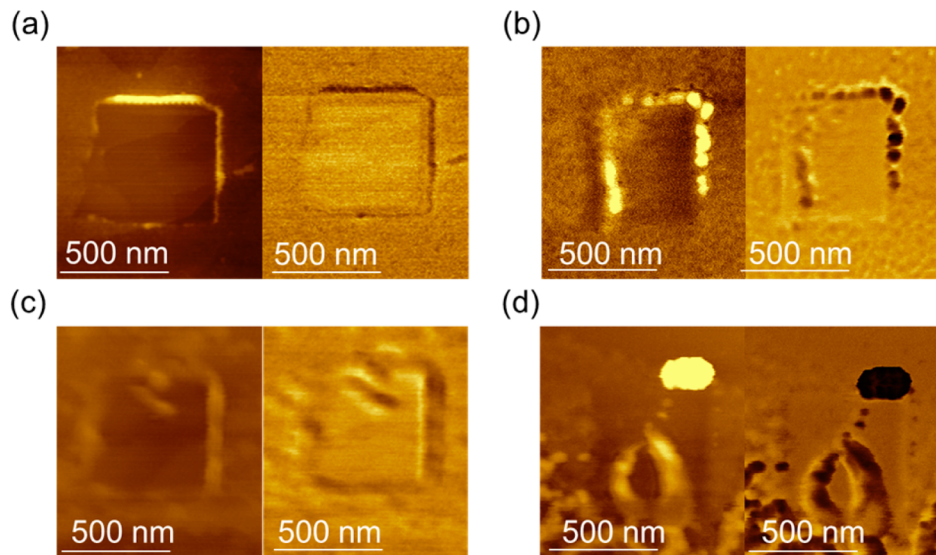


Figure 8. Topography images and tip–sample adhesion images of (a) PET/HOPG and (b) PET/mica at 40 °C and (c) PET/HOPG and (d) PET/mica at 90 °C after five successive abrasive raster scans. The difference in surface elevation between the brightest and darkest features is (a, c, d) 6 nm and (b) 4 nm.

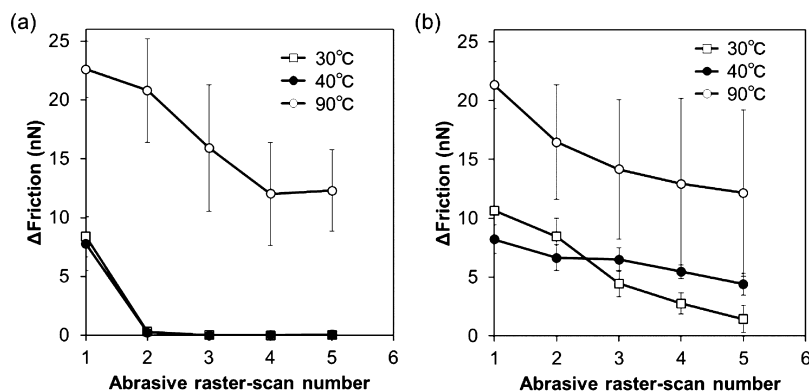


Figure 9. Δ Friction of (a) PET/HOPG and (b) PET/mica under the different temperatures at 15 nN.

film and the precursor layer of PET bound to the mica was stronger than the interfacial adhesion between PET and HOPG at 30 °C. Applying these results to the model in Figure 1, our results suggest that the *relevant* interfacial adhesion in PET/clay nanocomposites (i.e., between a presumed precursor layer and the bulk polymer) is markedly stronger than that in PET/graphene nanocomposites at 30 °C.

Effect of Temperature on Wear Response of PET Film on Substrate. Wear response was further characterized at two elevated temperatures, below T_g at 40 °C and above T_g at 90 °C, to assess the effect of glassy versus rubbery response on interfacial adhesion. It was first noted that atop PET films deposited on both substrate types the tip–sample adhesive force increased at 90 °C compared to the glassy state at 30–40 °C (see Figure S8 in Supporting Information), indicating that the tack of PET films increases above T_g . Figure 7 contains representative successive topography images of PET on HOPG and PET on mica during abrasive scanning (loading force 15 nN) at 40 and 90 °C. Figure 8 shows the ensuing larger topography and tip–polymer adhesion images: both PET/HOPG and PET/mica display similar behaviors at 40 °C as at 30 °C (previous section). At 90 °C, PET/HOPG and PET/mica exhibited a greater tendency to form bundles in the first abrasive raster scan, which then grew in height during repeated

scans. Consistent with this propensity for bundle formation *inside* of the abraded region at 90 °C, a lesser piling of PET at the *periphery* of the abraded region is observed at 90 °C on each substrate. These observations imply a more *cohesive failure* during abrasive scanning at 90 °C as compared to 30–40 °C.

Friction force characterization during abrasive scanning corroborates the above interpretation. Figure 9 plots the mean and standard deviation of Δ Friction (as defined in the preceding section, i.e., referenced to “bared” substrates) for both PET/HOPG and PET/mica and at 40 and 90 °C, superimposed with the results at 30 °C (distributions of F_f are shown in Figure S9 of the Supporting Information). Most notably, the glassy-regime behaviors are similar (i.e., 30 °C versus 40 °C), whereas at 90 °C both mean and standard deviations of Δ Friction are much greater. Downward trends with repeated raster scans are universally observed, but a dramatic drop in both mean and standard deviation from first to second raster scan is only exhibited in the glassy regime and only for the case of PET/HOPG. These observations are consistent with an interpretation of cohesive failure in all cases except for PET/HOPG in the glassy regime. These results further suggest that (1) the relevant interfacial adhesion in the PET/mica system (i.e., between *precursor layer and bulk polymer*) is stronger than that at the PET/HOPG interface at

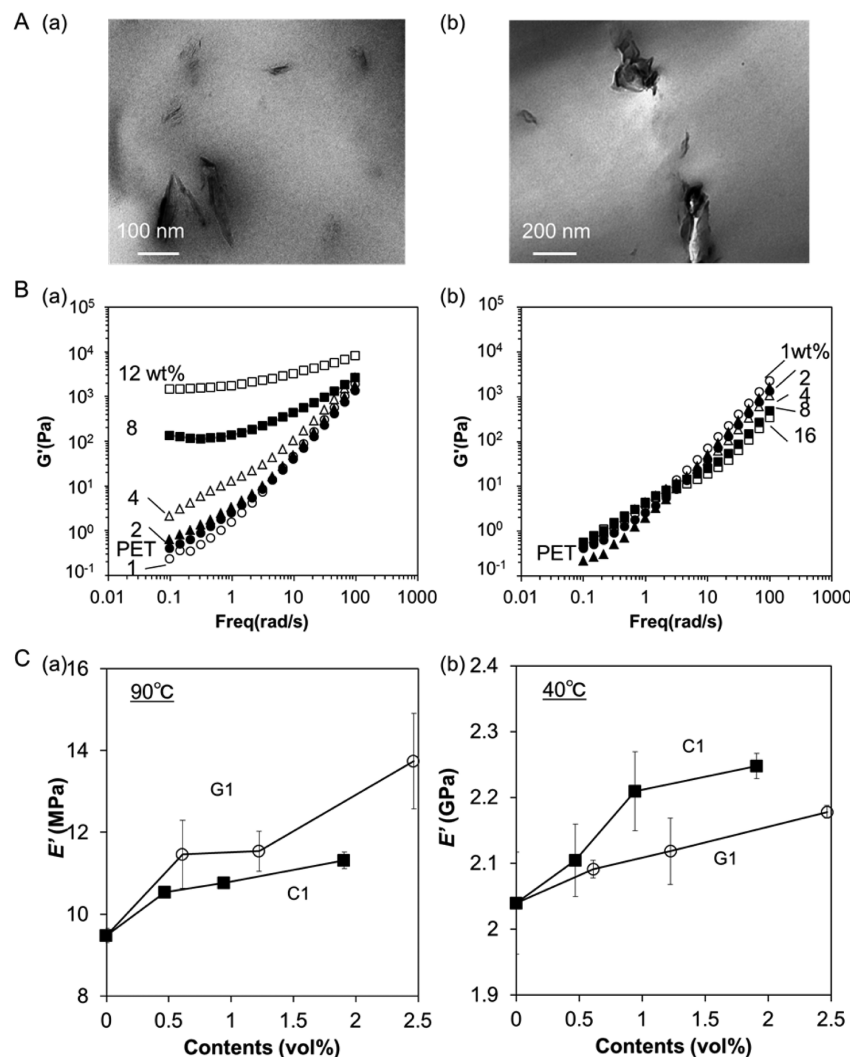


Figure 10. (A) TEM images of (a) PET/G1 and (b) PET/C1 with 2 wt % nanofillers. (B) Dynamic shear storage moduli, G' , of (a) PET/G1 and (b) PET/C1 at 270 °C at several loading levels. (C) Dynamic storage moduli, E' , of PET/G1 and PET/C1 at (a) 90 and (b) 40 °C.

30–40 °C (in the glassy dynamic regime) and (2) the ability of PET chains in the interfacial region to absorb shear stress at 90 °C in the rubbery dynamic regime of the bulk system was markedly increased compared to the glassy regime, such that the behavior differed little in the two laminates.

It is important to clarify our reference to rubbery versus glassy dynamics in the context of PET thin films. An AFM friction study of 12 nm PET films on SiO₂⁴⁴ reported a T_g of 50–55 °C, well below the bulk T_g of PET. An infrared spectroscopy study of 22 nm PET thin films on gold similarly reported a T_g of 49 °C.⁴⁵ The latter is an average value from the whole film, and the former may be affected by surface effects, but in both cases enhanced mobility is implied. On the other hand, polymer in the immediate vicinity of a substrate has been called a dead layer.^{46,47} The mobility of polymer in this dead layer is restricted due to interactions with the substrate, manifest as an increased T_g .³⁸ Our ~2 nm films are similar in thickness to a reduced-mobility interfacial region in (i) thin films as reported by Kim et al.³⁸ and (ii) bulk nanocomposites as reported by Sargsyan et al.³⁹ Therefore, we anticipate that the T_g of our PET thin films on both substrates is higher than 55 °C, but most likely is not higher than the bulk T_g of our initial polymer, 79 °C. We cannot state, however, that our

upper measurement temperature of 90 °C is definitively above the (unknown) T_g of our PET thin films. (Ongoing studies may shed light on this question.)

Mechanical Properties of PET-Based Nanocomposites. In order to assess the relationship between interfacial adhesion and mechanical properties, amorphous PET-based nanocomposites with different loadings of graphene (G1) and clay (C1) were prepared by melt processing. Dispersion was evaluated via TEM and rheology of the molten dispersions. TEM images, dynamic shear storage moduli, G' , of molten dispersion, and elastic tensile storage moduli, E' , of solid PET films are shown in Figure 10. Although some G1 aggregates were observed in PET/G1, graphene dispersed well, whereas large C1 aggregates were observed in PET/C1 (representative images in Figure 10A).

Figure 10B shows shear storage modulus vs frequency for different filler loadings. The upturn in G' at low frequency indicates that the particles have formed a sample spanning network.^{37,48} The low-frequency upturn in G' occurs between 4 and 8 wt % for G1, whereas there is no significant change in slope of G' up to 16 wt % for C1. These results suggest that G1 has a lower percolation threshold than C1, in agreement with the TEM images that graphene was better dispersed in PET.

Elastic tensile storage moduli, E' , of solid PET films at increasing loading levels of G1 and C1 are plotted in Figure 10C at 90 and 40 °C. At 90 °C PET is above its T_g and rubbery. The moduli of the graphene reinforced samples are slightly higher than for clay reinforcement. The friction force data for both HOPG and mica at 90 °C in Figure 9 are high and similar to each other, indicating that PET is sticky in both cases. Thus, the slightly higher moduli for G1 are likely due to its better dispersion as seen in the TEM images.

The moduli at 40 °C are much higher as the PET is glassy at this temperature, but the effect of reinforcement is smaller. This is partially due to the fact that when the matrix modulus is closer to the filler modulus the reinforcing effect decreases.^{11,49,50} However, much lower adhesion of G1 to PET causes lower stress transfer efficiency than does C1 at 40 °C. In fact, at 40 °C, clay increases the modulus of PET much more than graphene does, in good agreement with the AFM abrasion results in Figure 9.

Effect of Interfacial Adhesion on Mechanical Properties of PET-Based Nanocomposites. Li et al.⁵¹ reported that poly(butylene terephthalate) interacted with exfoliated graphite via $\pi-\pi$ interactions. Similarly, PET also can interact with graphene via $\pi-\pi$ interaction. The interaction between PET and clay or mica is through hydrogen bonds. The surface of mica and clay is negatively charged with hydroxyl groups.^{52,53} These hydroxyl groups are capable of making strong intermolecular interactions with terminal carboxylic groups and ester groups along PET chains.^{54,55} Generally, the energy of hydrogen bonds (15–40 kJ mol⁻¹) is higher than that of $\pi-\pi$ interactions (10 kJ mol⁻¹).⁵⁶ Benzene rings can also interact with mineral surfaces via cation– π interactions.⁵⁷ Therefore, per these concepts and our AFM measurements, PET chains apparently flatten on mica to form a precursor layer at the interface and similarly adhere more strongly to clay than to graphene in nanocomposites. At 90 °C, PET is above its bulk T_g and thus more mobile such that stress at the immediate PET/filler interface is relaxed. Thus, a possibly stronger interaction of PET with clay versus graphene has little influence compared to the viscoelasticity of the soft PET, similar to the tack observed in pressure-sensitive adhesives at temperatures above T_g .⁵⁸ Thus, there is little difference in the strength of interfacial adhesion between the two nanocomposites.

From the bulk mechanical measurements, graphene exhibited less stiffening in the glassy regime than clay despite better dispersion of graphene than clay. Weaker adhesion causes less immobilization of PET chains in the interfacial regions and a decrease in the stress transfer efficiency between matrix polymer and nanofillers,⁵⁹ most likely leading to more ductile behavior.⁶⁰ Therefore, the relatively weaker interfacial adhesion between PET and graphene in the glassy regime counteracts the effect of the superior material property and the dispersion level of graphene, resulting in a low stiffening effect. On the other hand, above T_g bulk PET becomes softer by 2 orders of magnitude compared to below T_g . Correspondingly, the difference between the moduli of nanofiller and matrix is much greater in the rubbery (bulk) dynamic regime. This large difference dominates the modulus increase as Kim et al.¹¹ have pointed out. The AFM-assessed interfacial adhesion in this regime differed little in the two nanocomposites, presumably due to enhanced chain mobility in the films compared to the low temperature state, thus suppressing the influence of chain–substrate interactions. Therefore, the superior material properties and the higher dispersion level of graphene result in the

higher moduli of PET/graphene nanocomposites compared to PET/clay in the rubbery regime.

■ SUMMARY AND CONCLUSIONS

In this work, we developed an atomic force microscopy (AFM)-based abrasive scanning methodology, applied to model laminate systems, to probe the strength of interfacial adhesion relevant to poly(ethylene terephthalate) (PET) nanocomposites in which graphene or clay platelets are dispersed. Graphite and mica substrates covered with ~2 nm thick PET films were abrasively sheared by an AFM tip as a model measurement of interfacial strength between matrix PET and dispersed graphene and clay, respectively, in nanocomposites. Below T_g , PET on graphite exhibited abrupt delamination (i.e., full adhesive failure) during raster scanning, whereas PET on mica exhibited cohesive failure. Moreover, 100-fold higher force scanning procedures were required to abrade through an ultimate “precursor” layer of PET only 0.2–0.5 nm thick, which must reside largely disentangled from the bulk matrix polymer. Below T_g , friction on PET/mica during abrasive scanning was higher than that on PET/HOPG. Above T_g , both laminates exhibited similar behavior, higher friction, and cohesive failure prior to interface delamination. These results suggest that in the glassy dynamic regime the relevant interfacial adhesion in PET/clay nanocomposites (i.e., between a presumed precursor layer and the bulk polymer) is stronger than that in PET/graphene nanocomposites, whereas in the rubbery dynamic regime (of the bulk system), the mobility of PET chains in the interfacial region is markedly increased such that the relevant interfacial adhesion differs little in the two nanocomposites. Bulk mechanical properties of the two nanocomposites are correlated with the differences in interfacial adhesion probed by AFM. The relatively weaker interfacial adhesion between PET and graphene in the glassy regime causes a decrease in the stress transfer efficiency, resulting in less increase in modulus despite better dispersion of graphene than clay. In the rubbery regime interfacial adhesion was similar for both fillers due to enhanced mobility of PET, thus even just following the simple mixture rules the better dispersed graphene resulted in a greater modulus increase. Our abrasive AFM scanning methodology can be applied to other nanocomposites to assess interfacial adhesion, including the assessment of bonding between polymer and surface modified nanofillers (using surface-modified substrates in laminate model systems).

■ ASSOCIATED CONTENT

S Supporting Information

Procedure for obtaining friction force, distribution of friction force, Δ Friction, abrasion of precursor layer, and tip–sample adhesive force on PET films. This material is available free of charge via the Internet at <http://pubs.acs.org>.

■ AUTHOR INFORMATION

Corresponding Author

*E-mail: haugs001@umn.edu (G.H.).

Notes

The authors declare no competing financial interest.

■ ACKNOWLEDGMENTS

This research was supported by Toray Industries through their membership in the University of Minnesota Industrial Partnership for Research in Interfacial and Materials Engineering

(IPRIME). Parts of this work were performed in the University of Minnesota Characterization Facility, which receives partial support from the NSF through the MRSEC program.

■ REFERENCES

- (1) Brune, D. A.; Bicerano, J. Micromechanics of nanocomposites: comparison of tensile and compressive elastic moduli, and prediction of effects of incomplete exfoliation and imperfect alignment on modulus. *Polymer* **2002**, *43*, 369–387.
- (2) Choi, W.; Kim, H.; Yoon, K.; Kwon, O.; Hwang, C. Preparation and barrier property of poly(ethylene terephthalate)/clay nanocomposite using clay-supported catalyst. *J. Appl. Polym. Sci.* **2006**, *100*, 4875–4879.
- (3) Hasegawa, N.; Kawasumi, M.; Kato, M.; Usuki, A.; Okada, A. Preparation and mechanical properties of polypropylene-clay hybrids using a maleic anhydride-modified polypropylene oligomer. *J. Appl. Polym. Sci.* **1998**, *67*, 87–92.
- (4) Tsai, T. Y.; Li, C. H.; Chang, C. H.; Cheng, W. H.; Hwang, C. L.; Wu, R. J. Preparation of exfoliated polyester/clay nanocomposites. *Adv. Mater.* **2005**, *17*, 1769–1773.
- (5) Sharma, R.; Joshi, H.; Jain, P. Short review on the crystallization behavior of PET/clay nanocomposites. *J. Chem. Eng. Mater. Sci.* **2011**, *2*, 39–43.
- (6) Ou, C.; Ho, M.; Lin, J. Synthesis and characterization of poly(ethylene terephthalate) nanocomposites with organoclay. *J. Appl. Polym. Sci.* **2004**, *91*, 140–145.
- (7) Vermogen, A.; Masenelli-Varlot, K.; Séguéla, R. Evaluation of the structure and dispersion in polymer-layered silicate nanocomposites. *Macromolecules* **2005**, *38*, 9661–9669.
- (8) Gökkurt, T.; Durmus, A.; Sariboga, V.; Öksüzömer, M. A. F. Investigation of thermal, rheological, and physical properties of amorphous poly(ethylene terephthalate)/organoclay nanocomposite films. *J. Appl. Polym. Sci.* **2013**, *129*, 2490–2501.
- (9) Geim, A. K.; Novoselov, K. S. The rise of graphene. *Nat. Mater.* **2007**, *6*, 183–191.
- (10) Novoselov, K. S.; Geim, A. K.; Morozov, S. V.; Jiang, D.; Katsnelson, M. I.; Grigorieva, I. V.; Dubonos, S. V.; Firsov, A. A. Two-dimensional gas of massless Dirac fermions in graphene. *Nature* **2005**, *438*, 197–200.
- (11) Kim, H.; Abdala, A. A.; Macosko, C. W. Graphene/polymer nanocomposites. *Macromolecules* **2010**, *43*, 6515–6530.
- (12) Kim, H.; Macosko, C. W. Processing-property relationships of polycarbonate/graphene composites. *Polymer* **2009**, *50*, 3797–3809.
- (13) Feng, R.; Guan, G.; Zhou, W.; Li, C.; Zhang, D.; Xiao, Y. In situ synthesis of poly(ethylene terephthalate)/graphene composites using a catalyst supported on graphite oxide. *J. Mater. Chem.* **2011**, *21*, 3931–3939.
- (14) Bandla, S.; Hanan, J. C. Microstructure and elastic tensile behavior of polyethylene terephthalate-exfoliated graphene nanocomposites. *J. Mater. Sci.* **2012**, *47*, 876–882.
- (15) Li, M.; Jeong, Y. G. Poly(ethylene terephthalate)/exfoliated graphite nanocomposites with improved thermal stability, mechanical and electrical properties. *Composites: Part A* **2011**, *42*, 560–566.
- (16) Li, M.; Jeong, Y. G. Influences of exfoliated graphite on structures, thermal stability, mechanical modulus, and electrical resistivity of poly(butylene terephthalate). *J. Appl. Polym. Sci.* **2012**, *125*, E532–E540.
- (17) Gómez-Navarro, C.; Burghard, M.; Kern, K. Elastic properties of chemically derived single graphene sheets. *Nano Lett.* **2008**, *8*, 2045–2049.
- (18) Lee, C.; Wei, X.; Kysar, J. W.; Hone, J. Measurement of the elastic properties and intrinsic strength of monolayer graphene. *Science* **2008**, *321*, 385–388.
- (19) Pitkethly, M. J.; Favre, J. P.; Gaur, U.; Jakubowski, J.; Mudrich, S. F.; Caldwell, D. L.; Drzal, L. T.; Nardin, M.; Wagner, H. D.; Landro, L. D.; Hampe, A.; Armistead, J. P.; Desaeger, M.; Verpoest, I. A round-robin programme on interfacial test methods. *Compos. Sci. Technol.* **1993**, *48*, 205–214.
- (20) Yue, C. Y.; Cheung, W. L. Interfacial properties of fibre-reinforced composites. *J. Mater. Sci.* **1992**, *27*, 3843–3855.
- (21) Herrera-Franco, P. J.; Drzal, L. T. Comparison of methods for the measurement of fibre/matrix adhesion in composites. *Composites* **1992**, *23*, 2–27.
- (22) Gong, L.; Kinloch, I. A.; Young, R. J.; Riaz, I.; Jalil, R.; Novoselov, K. S. Interfacial stress transfer in a graphene monolayer nanocomposite. *Adv. Mater.* **2010**, *22*, 2694–2697.
- (23) Li, Z.; Young, R. J.; Kinloch, I. A. Interfacial stress transfer in graphene oxide nanocomposites. *ACS Appl. Mater. Interfaces* **2013**, *5*, 456–463.
- (24) Robinson, I. M.; Zakikhani, M.; Day, R. J.; Young, R. J.; Galiotis, C. Strain dependence of the Raman frequencies for different types of carbon fibres. *J. Mater. Sci. Lett.* **1987**, *6*, 1212–1214.
- (25) Cooper, C. A.; Young, R. J.; Halsall, M. Investigation into the deformation of carbon nanotubes and their composites through the use of Raman spectroscopy. *Composites, Part A* **2001**, *32*, 401–411.
- (26) Young, R. J.; Gong, L.; Kinloch, I. A.; Riaz, I.; Jalil, R.; Novoselov, K. S. Strain mapping in a graphene monolayer nanocomposite. *ACS Nano* **2011**, *5*, 3079–3084.
- (27) Barber, A. H.; Cohen, S. R.; Wagner, H. D. Measurement of carbon nanotube–polymer interfacial strength. *Appl. Phys. Lett.* **2003**, *82*, 4140–4142.
- (28) Cai, M.; Glover, A. J.; Wallin, T. J.; Kranbuehl, D. E.; Schniepp, H. C. Direct measurement of the interfacial attractions between functionalized graphene and polymers in nanocomposites. *AIP Conf Proc.* **2010**, *1255*, 95–97.
- (29) Dvir, H.; Jopp, J.; Gottlieb, M. Estimation of polymer–surface interfacial interaction strength by a contact AFM technique. *J. Colloid Interface Sci.* **2006**, *304*, 58–66.
- (30) Dvir, H.; Gottlieb, M. Effect of silane sizing on polymer–glass adhesion. *ICCM17 proceedings 2007*, http://www.iccm-central.org/Proceedings/ICCM17_proceedings/The%20es/Materials/INTERPHASES%20&%20INTERFACES/D7.15%20Gottlieb.pdf.
- (31) Gupta, V. B.; Bashir, Z. *Handbook of Thermoplastic Polyesters: Homopolymers, Copolymers, Blends, and Composites*, 2005; DOI 10.1002/3527601961.ch7b.
- (32) Elenga, R.; Seguela, R.; Rietsch, F. Thermal and mechanical behaviour of crystalline poly(ethylene terephthalate): effects of high temperature annealing and tensile drawing. *Polymer* **1991**, *32*, 1975–1982.
- (33) Salem, D. R. Orientation and crystallization in poly(ethylene terephthalate) during drawing at high temperatures and strain rates. *Polym. Eng. Sci.* **1999**, *39*, 2419–2430.
- (34) Lu, X. F.; Hay, J. Crystallization orientation and relaxation in uniaxially drawn poly(ethylene terephthalate). *Polymer* **2001**, *43*, 8055–8067.
- (35) Mascia, L.; Fekkai, Z. Influence of stress-induced crystallization on the dimensional stability of monoaxially drawn poly(ethylene terephthalate). *Polymer* **1993**, *34*, 1418–1422.
- (36) Salem, D. R. Crystallization during hot-drawing of poly(ethylene terephthalate) film: influence of the deformation mode. *Polymer* **1995**, *36*, 3605–3608.
- (37) Aoyama, S.; Park, Y. T.; Ougizawa, T.; Macosko, C. W. Melt crystallization of poly(ethylene terephthalate): Comparing addition of graphene vs. carbon nanotubes. *Polymer* **2014**, DOI: 10.1016/j.polymer.2014.02.055.
- (38) Kim, J. H.; Jang, J.; Zin, W.-C. Thickness Dependence of the glass transition temperature in thin polymer films. *Langmuir* **2001**, *17*, 2703–2710.
- (39) Sargsyan, A.; Tonoyan, A.; Davtyan, S.; Schick, C. The amount of immobilized polymer in PMMA SiO₂ nanocomposites determined from calorimetric data. *Eur. Polym. J.* **2007**, *43*, 3113–3127.
- (40) Haugstad, G. *Atomic Force Microscopy: Understanding Basic Modes and Advanced Applications*; John Wiley & Sons: Hoboken, NJ, 2012.
- (41) Karthaus, O.; Gråsjö, L.; Maruyama, N.; Shimomura, M. Formation of ordered mesoscopic patterns in polymer cast films by dewetting. *Thin Solid Films* **1998**, *327–329*, 829–832.

- (42) Kumaki, J.; Hashimoto, T. Conformational change in an isolated single synthetic polymer chain on a mica surface observed by atomic force. *J. Am. Chem. Soc.* **2003**, *125*, 4907–4917.
- (43) Haugstad, G.; Gladfelter, W. L.; Weberg, E. B.; Weberg, R. T.; Weatherill, T. D. Probing biopolymers with scanning force methods: Adsorption structure, properties, and transformation of gelatin on mica. *Langmuir* **1994**, *10*, 4295–4306.
- (44) Hammerschmidt, J. A.; Gladfelter, G. L.; Haugstad, G. Probing polymer viscoelastic relaxations with temperature-controlled friction force microscopy. *Macromolecules* **1999**, *32*, 3360–3367.
- (45) Zhang, Y.; Zhang, J.; Lu, Y.; Duan, Y.; Yan, S.; Shen, D. Glass transition temperature determination of poly(ethylene terephthalate) thin films using reflection-absorption FTIR. *Macromolecules* **2004**, *37*, 2532–2537.
- (46) Napolitano, S.; Prevosto, D.; Lucchesi, M.; Pingue, P.; D'Acunto, M.; Rolla, P. Influence of a reduced mobility layer on the structural relaxation dynamics of aluminum capped ultrathin films of poly(ethylene terephthalate). *Langmuir* **2007**, *23*, 2103–2109.
- (47) Fukao, K.; Miyamoto, Y. Slow dynamics near glass transitions in thin polymer films. *Phys. Rev. E* **2001**, *64*, 011803–1–011803-9.
- (48) Vermant, J.; Ceccia, S.; Dolgovskij, M. K.; Maffettone, P. L.; Macosko, C. W. Quantifying dispersion of layered nanocomposites via melt rheology. *J. Rheol.* **2007**, *51*, 429–450.
- (49) Mori, T.; Tanaka, K. Average stress in matrix and average elastic energy of materials with misfitting inclusions. *Acta Metall.* **1973**, *21*, 571–574.
- (50) Tandon, G. P.; Weng, G. J. The effect of aspect ratio of inclusions on the elastic properties of unidirectionally aligned composites. *Polym. Compos.* **1984**, *5*, 327–333.
- (51) Li, M.; Jeong, Y. G. Influences of exfoliated graphite on structures, thermal stability, mechanical modulus, and electrical resistivity of poly(butylene terephthalate). *J. Appl. Polym. Sci.* **2012**, *125*, E532–E540.
- (52) Pashley, R. M. Hydration forces between mica surfaces in aqueous electrolyte solutions. *J. Colloid Interface Sci.* **1981**, *80*, 153–163.
- (53) Bezanilla, M.; Manne, S.; Laney, D. E.; Lyubchenko, Y. L.; Hansma, H. G. Adsorption of DNA to mica, silylated mica, and minerals: Characterization by atomic force microscopy. *Langmuir* **1995**, *11*, 655–659.
- (54) Gashti, M. P.; Moradian, S. Effect of nanoclay type on dyeability of polyethylene terephthalate/clay nanocomposites. *J. Appl. Polym. Sci.* **2012**, *125*, 4109–4120.
- (55) Parvinzadeh, M.; Moradian, S.; Rashidi, A.; Yazdanshenas, M.-E. Surface characterization of polyethylene terephthalate/silica nanocomposites. *Appl. Surf. Sci.* **2010**, *256*, 2792–2802.
- (56) Roesky, H. W.; Andruh, M. The interplay of coordinative, hydrogen bonding and $\pi-\pi$ stacking interactions in sustaining supramolecular solid-state architectures.: A study case of bis(4-pyridyl)- and bis(4-pyridyl-N-oxide) tectons. *Coord. Chem. Rev.* **2003**, *236*, 91–119.
- (57) Zhu, D.; Herbert, B. E.; Schlautman, M. A.; Carraway, E. R.; Hur, J. Cation- π bonding. *J. Environ. Qual.* **2004**, *33*, 1322–1330.
- (58) Zosel, A. Adhesion and tack of polymers: Influence of mechanical properties and surface tensions. *Colloid Polym. Sci.* **1985**, *263*, 541–553.
- (59) Schadler, L. S.; Giannaris, S. C.; Ajayan, P. M. Load transfer in carbon nanotube epoxy composites. *Appl. Phys. Lett.* **1998**, *73*, 3842–3844.
- (60) Nie, S.; Basaran, C. A micromechanical model for effective elastic properties of particulate composites with imperfect interfacial bondes. *Int. J. Solids Struct.* **2005**, *41*, 4179–4191.